

Terminal velocities of a deformed Leidenfrost liquid: Experiments and self-propulsion model

Guanqi Wang,¹ Jonathan McDonough ,¹ Vladimir Zivkovic,¹ Teng Long,²
Zuankai Wang,³ and Steven Wang ^{3,*}

¹*School of Engineering, Newcastle University, NE1 7RU, United Kingdom*

²*School of Engineering, University of Cambridge, CB2 1TN, United Kingdom*

³*Department of Mechanical Engineering, City University of Hong Kong, Hong Kong, 999077, China*



(Received 20 January 2021; accepted 7 January 2022; published 14 March 2022)

We derive a model entirely from first principles to explain the Leidenfrost self-propulsion phenomenon in a quantitative way, where the deformable nature of the liquid has been taken into account. Experiments show a good agreement with our model, suggesting this model supersedes the limited scaling analysis previously given in the literature. Our annular ring design enables liquid droplets to reach high terminal velocities, up to 0.42 ± 0.04 m/s, which is potentially beneficial to energy harvesting and flow chemistry applications.

DOI: [10.1103/PhysRevFluids.7.033602](https://doi.org/10.1103/PhysRevFluids.7.033602)

I. INTRODUCTION

On a ratcheted surface, a Leidenfrost droplet (solid) will self-propel as first reported by Linke *et al.* in 2006 [1]. Since then, the origin for the phenomenon has been debated [2–5], and there has not yet been a first-principles model description that neither matches nor explains experimental observations. The viscous mechanism due to a pressure-driven vapor flow appears to be the dominant phenomenon behind droplet self-propulsion [4,6]. Some quantitative understanding of the motion has also been obtained by neglecting liquid deformation by replacing the liquids with rigid Leidenfrost solids (e.g., dry ice) [7]. Although this latter study provides a 3D description of the flow field, the error between the experimental data and model predictions is still subject to further interpretation. Ultimately, the development of a liquid droplet model is still lacking, affecting the progress of potential applications of these Leidenfrost devices such as their use as heat engines to generate electricity [8,9], or to drive fluid mixing in flow chemistry applications.

In this paper, we propose an analytical model that can be generally used to describe the self-propulsion phenomenon. Herein, the liquid deformation at the presence of ratchets will be taken into account. A detailed force analysis in response to the deformation has been characterized in order to find a quantitative description of the driving force. Our model supersedes the limited scaling analysis already conducted in the literature [4] by revealing how the ratchet geometry influences the driving force, showing the individual influence of droplet size, ratchet design, operating temperature, and liquid deformation on the dynamics of the motion. This enables optimization of the experimental conditions for any given ratchet design. This annular design (Fig. 1) enables large liquid slugs to self-propel at higher velocities than simpler linear ratcheted surfaces, producing much larger kinetic energies. This quantitative model will guide the construction of Leidenfrost devices for use as heat engines to generate electricity [8,9], or for flow chemistry applications where low-volume liquid

*steven.wang@cityu.edu.hk

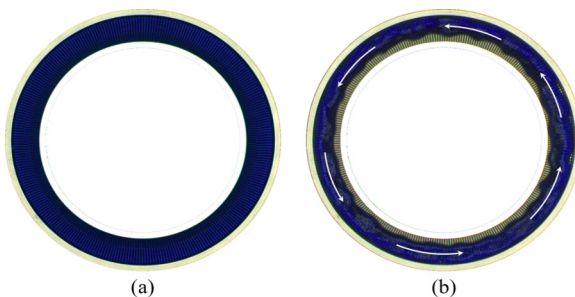


FIG. 1. (a) At 20 °C, no liquid flow is observed on a ratcheted ring; (b) At 400 °C, a vapor film forms beneath the liquid that suspends it; interaction of the vapor with the textured surface then creates motion with a terminal velocity of $\sim 0.42 \pm 0.04$ m/s (Supplementary video 1; see Ref. [10]).

droplets containing reactants can be collided at high speeds. Our Supplementary video visualizes the concept (see Ref. [10]).

II. ANALYTICAL MODEL

To derive a model, we first consider a single groove with a width of λ and height of ε (Fig. 2), where a Cartesian coordinate system is set up with x parallel to the slope of the ratchet and y perpendicular to the slope. In this cross-sectional view, point C represents the lowest point of the liquid within each ratchet, dividing the deformation into two parts. Arc AC follows the slope of the ratchet, and is responsible for producing the directed vapor flow that drags the droplet. Arc BC hangs over the vertical step of the ratchet; the evaporated vapor here mainly flows downwards, then into and out of the plane of the diagram [1,4]. C_1 and C_2 are used to describe the resulting proportions of AC and BC , since point C can fall anywhere between A and B .

The pressure-driven vapor flow along the line AC behaves as a Poiseuille flow [1,4,11,12]. It is assumed to be incompressible with constant density ρ_v and viscosity μ , and the velocity distribution of the vapor flow is described by the Navier-Stokes equations at steady state (considering just the x direction). The shear stress between the vapor and droplet induces droplet motion. This stress is obtained from the velocity distribution between the lower edge of the droplet and the surface of the ratchet. We can derive an expression for this velocity distribution u_x by solving the continuity and Navier-Stokes equations using the no-slip boundary condition [13], allowing us to then write the shear stress as shown in Eq. (1) (see Supplemental Material for all steps of this derivation in

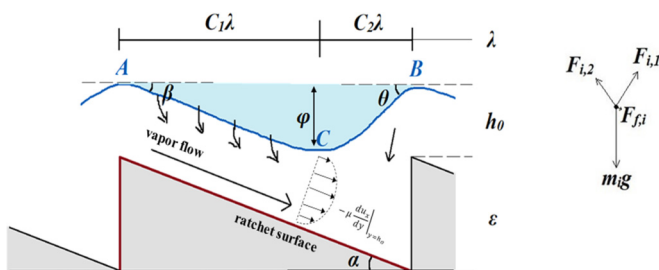


FIG. 2. Sketch of a single ratchet period. The droplet sits a distance of h_0 above the ratchet. The droplet has two deformation angles of β and θ , and a deformation depth of ϕ . The ratchet has a period of λ and depth of ε . The ratchet period varies from the inner edge (λ_i) to the outer edge (λ_o), which is a consequence of the ring design (see Fig. 1), while the ratchet height (ε) is fixed.

Ref. [10]):

$$F_{f,i} = -\mu \frac{du_x}{dy} A_{i,1} \Big|_{y=h_o} = -\frac{1}{2} A_{i,1} \left(\frac{\partial P}{\partial x} - \rho_v g_x \right) h_o - \frac{\mu v}{h_o} A_{i,1}. \quad (1)$$

Here, $A_{i,1}$ is the effective contact area of the deformed liquid lying on the slope of a single ratchet, $\partial P/\partial x$ is the pressure gradient that induces the vapor flow along the slope AC , gravitational acceleration is influenced by the gradient of the ratchet ($g_x = g \sin \alpha$), and v is the droplet's velocity. $A_{i,1}$ itself can be expressed as $w_{i,1} C_1 \lambda / \cos \beta$ where $w_{i,1}$ is the width of the droplet into and out of the plane shown in Fig. 2.

The overpressure ΔP is generated by the weight force [14]. We can assume the pressure around point C is close to atmospheric pressure because of the exposure to the atmosphere in the spacious ratchet corners. Figure 2 shows the directions of the different forces acting on the droplet. $F_{i,1}$ and $F_{i,2}$ are the forces exerted perpendicular to the lines AC and BC , respectively, as the vapor is expelled from the droplet. The weight force acting downward due to gravity is simply $m_i g$. We find that the driving force (i.e., shear stress, $F_{f,i}$) becomes negligible when compared to the much larger weight force. For example, a droplet of $30 \mu\text{L}$ weighs $\sim 300 \mu\text{N}$ while its net driving force is only $\sim 17 \mu\text{N}$ [2]. This means the deformation is mainly caused by gravity [14] since the shear force caused by the viscosity has little effect. By applying a force balance analysis, we then derive an expression for the pressure gradient [15] (also see Supplemental Material for more detailed analysis, Eqs. (S6)–(S10) in Ref. [10]):

$$\frac{dP}{dx} \approx -\frac{m_i g \sin \theta}{\sin(\theta + \beta) \left(\frac{w_{i,1} C_1 \lambda}{\cos \beta} \right) \left(\frac{C_1 \lambda}{\cos \beta} \right)}. \quad (2)$$

The total horizontal driving force is the sum of the individual driving forces generated within each ratchet period that the droplet covers ($F_f = \sum F_{f,i} \cos \beta$). By further considering the deformation geometry given in Fig. 2 [16], we obtain the following first-principles model for the driving force:

$$F_f = \frac{gh_o}{2} \left(\frac{M}{\lambda} + \rho_v A \frac{\sin \alpha \sin \theta}{\sin(\theta + \beta)} \right) \cos \beta - \frac{\mu A}{h_o} \frac{\sin \theta \cos \beta}{\sin(\theta + \beta)} v. \quad (3)$$

Here, M is the total mass of the droplet and A is the total area of the ratchets covered by the droplet as viewed from above. This area (A) can either be measured experimentally or approximated for large droplets by assuming that the ratio of the volume to height V/H_L will remain constant [17,18]. This expression shows that the driving force is dependent upon the liquid (vapor) properties (A , M , θ , β , ρ_v , h_o , and μ), ratchet geometric parameters (λ and α), gravity (g), and the droplet's velocity v (which itself is influenced by the aforementioned parameters).

If we assume the side view of the deformed droplet is triangular (so that ABC is triangular; see Fig. S1(a) in the Supplemental Material) and l_1 and l_2 represent the lengths of the deformed sides AC and BC , respectively, according to the law of sines it follows that $l_1 / \sin \theta = \lambda / \sin(\pi - [\theta + \beta])$, meaning $\sin \theta / \sin(\theta + \beta) = l_1 / \lambda \leq 1$. Hence, the second term in Eq. (3) has a maximum value of $\rho_v A \sin \alpha$, where ρ_v is $0.42\text{--}0.46 \text{ kg/m}^3$ for surface temperatures of $300\text{--}400 \text{ }^\circ\text{C}$. We then find that the first term in Eq. (3) is around 4 orders of magnitude larger than the second term, considering ρ_L is $\sim 10^3 \text{ kg/m}^3$ at its boiling point, $H_L \sim 4\text{--}5 \text{ mm}$, and $\lambda \sim 1 \text{ mm}$. Therefore, Eq. (3) can be simplified to Eq. (4):

$$F_f = \frac{Mgh_o \cos \beta}{2\lambda} - \frac{\mu A l_1}{h_o \lambda} v \cos \beta. \quad (4)$$

Now we consider the velocity term in Eq. (4). When the surface temperature is $\sim 400 \text{ }^\circ\text{C}$, the droplet's temperature is $\sim 100 \text{ }^\circ\text{C}$, and the temperature of the vapor flow is taken to be an average of the two: $250 \text{ }^\circ\text{C}$. Then, the vapor viscosity μ is $\sim 1.82 \times 10^{-5} \text{ Pa s}$, the vapor thickness h_o is $\sim 100 \mu\text{m}$ [1,2], and the ratchet period λ is $\sim 1 \text{ mm}$. Experimentally, the ultimate droplet velocity v is no more than 0.4 m/s .

For a 30- μL droplet with corresponding contact area (A) of $\sim 15.4 \text{ mm}^2$, the driving force due to the mass term in Eq. (19) is 15 μN , whereas the velocity term is only 0.8 μN . Similarly, for a larger droplet of 580 μL (with $A \sim 135.6 \text{ mm}^2$), experimentally the mass term in Eq. (19) is 270 μN , whereas the velocity term is 7.4 μN . Accordingly, if the velocity term in Eq. (4) is neglected, the same scaled expression of the model analysis for a rigid solid is obtained [4], this time derived from first principles:

$$F_f = \frac{Mgh_o \cos \beta}{2\lambda}. \quad (5)$$

To avoid measuring h_o experimentally, we can predict it using a simple mass balance. First, the mass lost from the droplet over time is equal to the heat-transfer rate across the vapor film (described by Fourier's law [2]) divided by the latent heat [Eq. (6)]. Here, the assumption of $\beta \sim \alpha$ is applied [as supported by the deformation analysis below; see Eqs. (13) and (14)]. Second, the mass lost from the droplet is also equal and opposite to the vapor mass flow rate, which is given by Eq. (7) below:

$$\frac{dm_{i,1}}{dt} = -\frac{\kappa}{L_L} \frac{\Delta T}{h_o} A_{i,1}, \quad (6)$$

$$\frac{dm_{i,1}}{dt} = -\rho_v \bar{u}_x w_{i,1} h_o. \quad (7)$$

Here, κ is the thermal conductivity of the vapor, L_L is the latent heat of evaporation, ΔT is the temperature difference between the base of the droplet and the ratchet surface, and \bar{u}_x is defined as the weighted-average flow velocity expressed as

$$\bar{u}_x = \frac{1}{h_o} \int_0^{h_o} u_x dy. \quad (8)$$

Combining Eqs. (6)–(8) will give the thickness of the vapor flow (where we have assumed that the “ vy/h_o ” term is negligible as discussed above):

$$h_o = C(T)^{1/4} \left(\frac{A_i \sin^2 \theta}{m_i \sin^2(\theta + \beta) + \rho_v A_i \lambda \sin \alpha \sin \theta \sin(\theta + \beta)} \right)^{1/4} \lambda^{1/2}. \quad (9)$$

Here, $C(T)$ describes the temperature-dependent properties of the vapor flow and the gravitational acceleration constant ($= 12\mu\kappa \Delta T / \rho_v g L_L$). The same simplifying assumptions made to Eq. (3) can also be applied to Eq. (9), leading to

$$h_o = C(T)^{1/4} \left(\frac{A \sin^2 \theta}{M \sin^2(\theta + \beta)} \right)^{1/4} \lambda^{1/2}. \quad (10)$$

For large droplets with a constant droplet height, the mass can be simply approximated by the density multiplied by the volume ($M = \rho_L H_L A$). Substituting Eq. (10) into Eq. (5) gives the driving force:

$$F_f = \frac{Mg}{2} \lambda^{-1/2} C(T)^{1/4} \left(\frac{A}{M} \right)^{1/4} \left(\frac{\sin \theta \cos^2 \beta}{\sin(\theta + \beta)} \right)^{1/2}. \quad (11)$$

The corresponding expression for droplet acceleration is simply obtained from Newton's second law (i.e., $F = Ma$):

$$a = \frac{g}{2} \lambda^{-1/2} C(T)^{1/4} \left(\frac{A}{M} \right)^{1/4} \left(\frac{\sin \theta \cos^2 \beta}{\sin(\theta + \beta)} \right)^{1/2}. \quad (12)$$

Assuming that the curve AC closely follows the shape of the slope of the ratchet, we have $\varphi \sim C_1 \varepsilon$ according to similar triangles, from which we arrive at a slightly alternative expression for the driving force and acceleration shown in Eqs. (13) and (14):

$$F_f = C_1^{1/2} \frac{Mg}{2} C(T)^{1/4} \left(\frac{A}{M} \right)^{1/4} \left(\frac{1}{\lambda^2 + \varepsilon^2} \right)^{1/4}, \quad (13)$$

$$a = C_1^{1/2} \frac{g}{2} C(T)^{1/4} \left(\frac{A}{M} \right)^{1/4} \left(\frac{1}{\lambda^2 + \varepsilon^2} \right)^{1/4}. \quad (14)$$

Now we consider the droplet deformation. Surface tension acts along the curved liquid-vapor interface and produces a force of $\int \gamma dl$ acting parallel to the interface. Here, γ represents the surface tension and dl refers to a small segment of the length of the curved liquid-vapor interface. The horizontal component of the force generated along arc BC will be balanced by the horizontal component of the surface tension force generated along arc AC . There will also be a net vertical component to this force, which can be defined with respect to either arc AC or arc BC . For example, the vertical force component of the surface tension acting along the arc BC can be expressed as $\int \sin \theta \gamma dl_2$, where l_2 refers to the length along the liquid-vapor interface between points B and C . Assuming that the surface tension is constant, this integrates to give a vertical force of $\gamma \varphi$ (where $\varphi = \int \sin \theta dl_2$ based on simple trigonometry; see Fig. 2). If we assume that the BC arc is approximately circular, then we can calculate the effective cross-sectional area of the droplet as $0.5\pi(C_2\lambda)^2$ (i.e., approximately half the area of a circle— πr^2 , where $r = C_2\lambda$). By dividing the vertical force component by this area, we can calculate the Laplace pressure induced by the surface tension. This Laplace pressure will then oppose the droplet's hydrostatic pressure ($\rho_L g H_L$) and dynamic pressure ($1/2 \rho_L v^2$) according to Eq. (15). From this equation, we can predict the values of C_2 and $C_1 (= 1 - C_2)$ without the need for any empirical observation.

$$\rho_L g H_L + \frac{\rho_L v^2}{2} = \frac{\gamma \varphi}{0.5\pi(C_2\lambda)^2}. \quad (15)$$

For example, the droplet velocity is $v \sim 0\text{--}0.4$ m/s according to our experiments. Thus, for a ratchet with $\lambda \sim 1$ mm and $\varepsilon \sim 0.5$ mm (where $H_L = 5$ mm [17,18] and $\varphi \sim C_1 \varepsilon$ as already mentioned), it is predicted that $C_1 \sim 0.46\text{--}0.62$. The deformed proportion then increases to $C_1 \sim 0.59\text{--}0.72$ when the ratchet ratio increases to $\lambda : \varepsilon = 1.5 \text{ mm} : 0.5 \text{ mm}$.

Equations (13) and (14) suggest that the driving force and acceleration are not only dependent on droplet radius (height) [2,4], but also on the ratchet geometry, the surface temperature, and the liquid deformation into the grooves of the ratchets. In practice though, both the driving force and acceleration are insensitive to the droplet height and temperature, because $C(T)^{1/4}$ and $(A/M)^{1/4}$ will remain relatively constant over a large temperature range (100°C). Therefore, on a ratcheted surface, the driving force should be a function of the droplet radius R alone, with an exponent of ~ 2 [which comes from replacing the first term in Eq. (13) with $M = \rho_L \pi R^2 H_L$, for large droplets with flattened shape]. Following this, the model predicts that the acceleration will be similar for droplets with different volumes. Our model is also internally consistent. For instance, if we set the deformed angles θ and β to 0, then Eq. (11) collapses to the form of Eq. (5), which is the same model derived for rigid nondeformable models (such as a disk of dry ice) [4].

We can also extend our driving force model [Eq. (13)] to predict the terminal velocity by considering the friction analysis previously presented [19]. The result shown in Eq. (16) only considers the friction as a result of the loss of kinetic energy, since the potential-energy barrier is less significant [19]. Here, b is an empirical coefficient requiring experimental observation that represents the significance of friction. Assuming that the empirical coefficient b is comparable over a few aspect ratios (λ/ε) [19], Eq. (16) predicts that a smaller ratchet (i.e., with smaller λ and ε) with larger aspect ratio (i.e., larger λ/ε) will produce a larger droplet velocity. The ratchet ratio

TABLE I. Summary of ring geometries used in this study.

Ring design	Outer diameter (mm)	Inner diameter (mm)	Ratchet shape	λ (mm)	λ_e^a (mm)	ε (mm)	Flat top length (mm)
1			o ^b 	1.05	1.05		
			i 	0.85	0.85		
2	103	83	o 	1.14	0.87	0.5	0.27
			i 	0.91	0.86		
3			o 	3	3		
			i 	2.41	2.41		
4	38	18	o 	1.07	0.79	0.4	0.28
			i 	0.5	0.5		

^a λ_e is the effective ratchet period of trapezium-shaped steps ($\lambda_e = \lambda - |\text{flat top length}|$).

^bo and i represent the outer and inner edges of the annular ring, respectively.

dominates the effect due to its larger index.

$$v = C_1^{-1/4} \left(\frac{gH_L}{2b} \right)^{1/2} \left(\frac{C(T)A}{M} \right)^{1/8} \left(\frac{\lambda}{\varepsilon} \right)^{1/2} \left(\frac{1}{\lambda^2 + \varepsilon^2} \right)^{1/8}. \quad (16)$$

A simple validation of the driving force model can be performed by using data already published in the literature [2]. Our model [Eq. (13)] predicts that the driving force should be proportional to the droplet radius to the power of 2. Supplemental Material, Fig. S2 confirms that the gradient of the droplet radius vs measured force data is 1.78 ± 0.24 , which is within experimental error (see Ref. [10]). Note that the Supplemental Material document details every step of the model derivation in detail.

III. EXPERIMENT

Experiments were subsequently performed using deionized water droplets on aluminum ratched rings. The use of rings instead of linear ratched surfaces, as commonly used in the literature, enables the terminal velocity to be reached in a much smaller footprint. In total, four different ring designs were used in the experiments, whose geometric parameters are summarized in Table I. The ratchets were either triangular or trapezoidal (having a “flat top”).

The rings were heated to 450, 400, 350, and 300 °C using a hot plate, and large droplets were deposited onto the surface via a micropipette with an initial negative velocity (moving from right to left with respect to Fig. 2). These droplets would then rapidly decelerate, before coming to a stop, then accelerate to positive velocities (moving from left to right in Fig. 2). This method enabled us to remove experimenter bias from the acceleration measurements (the droplets will all be accelerating from an initial velocity of 0 m/s). The droplet motion was investigated using a high-speed camera that recorded image sequences with a 20-ms time-step size. Droplet velocities (v), top-down contact areas (A), and acceleration (a) were subsequently available via image analysis. IMAGEJ (Fiji) [20] and a custom MATLAB program were used to automatically detect the moving droplets by tracking the center of mass. The initial slopes of the velocity-time graphs were taken as the acceleration (as shown in Fig. S3), since the initial droplet friction due to kinetic energy losses was negligible [19].

IV. RESULTS AND DISCUSSION

The droplet shape in the top-down view was typically elliptical rather than circular as shown in Fig. 3(a) (0.5–1.1s after deposit). Here the liquid spread in the direction of self-propulsion in

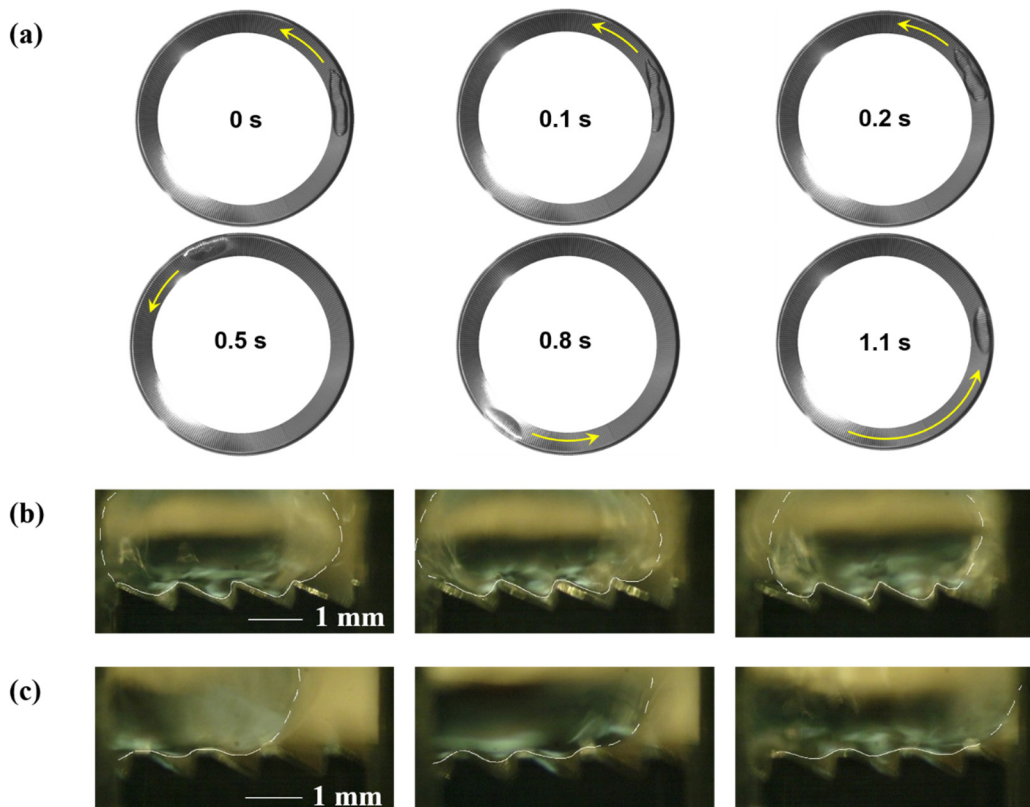


FIG. 3. (a) Top-down view of a Leidenfrost droplet ($600\text{-}\mu\text{L}$ volume) on ring design 1. In the initial acceleration period, the droplet spreads with irregular shape because of the considerable driving force of this ratchet design. Quickly the shape then became regular and formed an ellipse. (b), (c) Microscope images showing liquid deformation on ratcheted substrates at various times (t_0, t_1, t_2): (b) $\lambda_o > \varepsilon$, and (c) $\lambda_{e,o} \sim \varepsilon$.

accordance with the shear force direction. Specifically, on ring design 1 the high driving force caused the droplets to become elongated and flattened during the initial acceleration period, developing an irregular shape as shown in Fig. 3(a) (0–0.2 s). Here, the contact area is considerably enlarged, further increasing the driving force and acceleration according to Eqs. (16) and (17). The droplet shape then becomes regular after a short period because the driving force weakens as the droplet velocity increases [as shown in Fig. 3(a), 0.2–1.1 s].

Under film-boiling conditions on a flat surface, a vapor pocket will become trapped beneath the droplet, making it unstable [18], whereas the ratcheted texture of the rings enables this vapor to escape laterally within the grooves, improving the stability of the droplets. The deformation of a droplet on two different ratcheted substrates is shown in Figs. 3(b) and 3(c). Figure 3(b) corresponds to a ring with triangular-shaped ratchets, while Fig. 3(c) corresponds to a ring with trapezium-shaped ratchets (with $\lambda_{e,o} \sim \varepsilon$). On the triangular ratchets, the ratchet period (λ_o) is apparently larger than the ratchet height (ε), and we find that $C_1 \sim 0.67$ [by manually measuring the angles from Fig. 3(b)]. Alternatively, on the trapezium-shaped ratchets (Fig. 3), we find that $C_1 \sim 0.5$ where the ratchets were narrow (deep).

Figures 4(a)–4(d) compare the experimental results with the model for all four ring designs. Using Eq. (15), if we neglect the dynamic pressure, the deformation lengths C_1 for the four rings are predicted to be 0.50, 0.46, 0.78, and 0.40, respectively. If we include the dynamic pressure, these then increase to 0.66, 0.63, 0.83, and 0.57, respectively. These predictions are mostly in the range

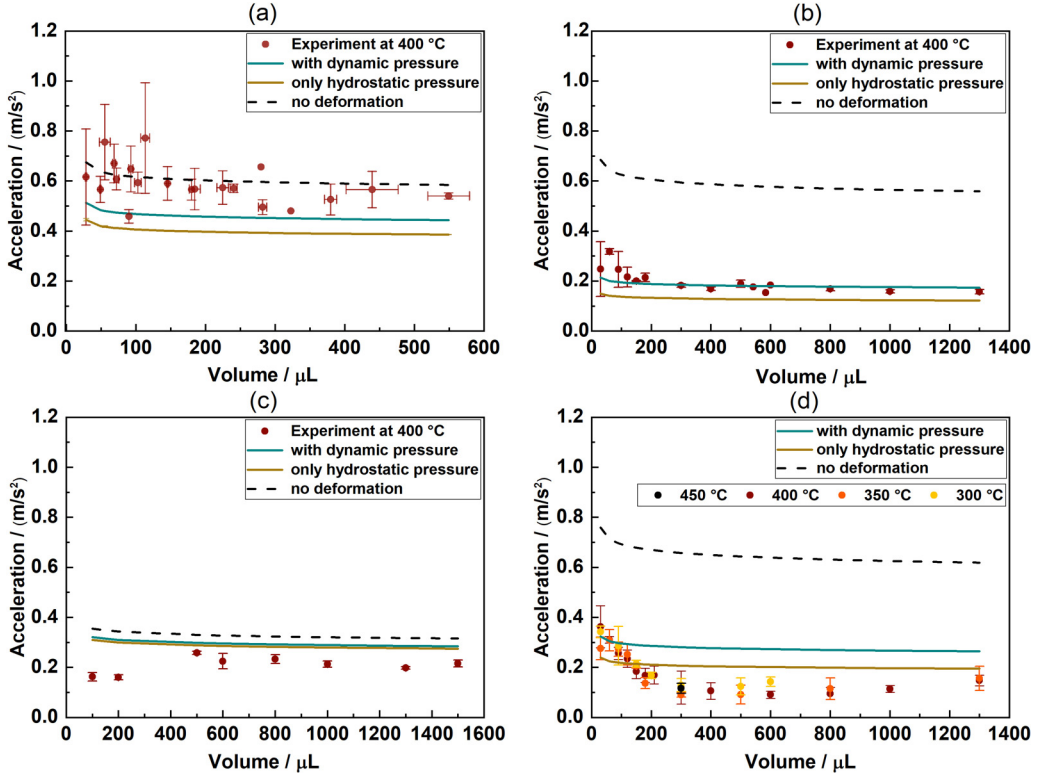


FIG. 4. Effect of droplet volume on initial acceleration. Each group of data was repeated at least three times. (a) Ring design 1 (400 °C), (b) ring design 2 (400 °C), (c) ring design 3 (400 °C), and (d) ring design 4 (450C, 400C, 350,C and 300 °C). Figure S7 shows the separate models on the large deviation on ring design 4.

of the experimental observations, and the model was subsequently plotted based on both sets of C_1 values. Additionally, for comparison, we also plotted the model assuming no deformation of the droplet at all (comparable to the behavior of a dry-ice disk), where we apply $\theta = \beta = 0$ in Eq. (11). It can be seen that the experiment data more closely match the prediction of the model when droplet deformation is considered.

It must be noted that when small droplets were deposited on the ring, they tended to settle at the inner edge as they transitioned from the initial negative velocity to a positive velocity. Then, as these started to accelerate in the “positive” direction, centrifugal force caused them to move to the outer edge following the trajectory sketched in Fig. S6(a). Thus, it is possible that the driving force continuously changed during this short period because of the changing ratchet parameters (as described above, the ratchets were narrower at the inner edge—so the driving force at the inner edge is different from the driving force at the outer edge). In contrast, the larger droplets tended to fill the full annular width of the ring [Fig. S6(b)], so the average ratchet properties did not change during acceleration. Therefore, we have plotted the model using the average of the ratchet geometric parameters at the inner and outer peripheries of the ring to account for this behavior. We see that the larger volumes more closely match the prediction of the model, since these larger droplets were pinned at the same radius, so did not experience the transition from inner- to outer-edge dimensions like the smaller droplets.

The largest deviation between experiment data and the model occurred for ring design 1 [Fig. 4(a)], and we believe that the elongation effect observed in Fig. 3(a) might explain this behavior. That is, the droplets became temporarily stretched out, causing them to flatten and increase

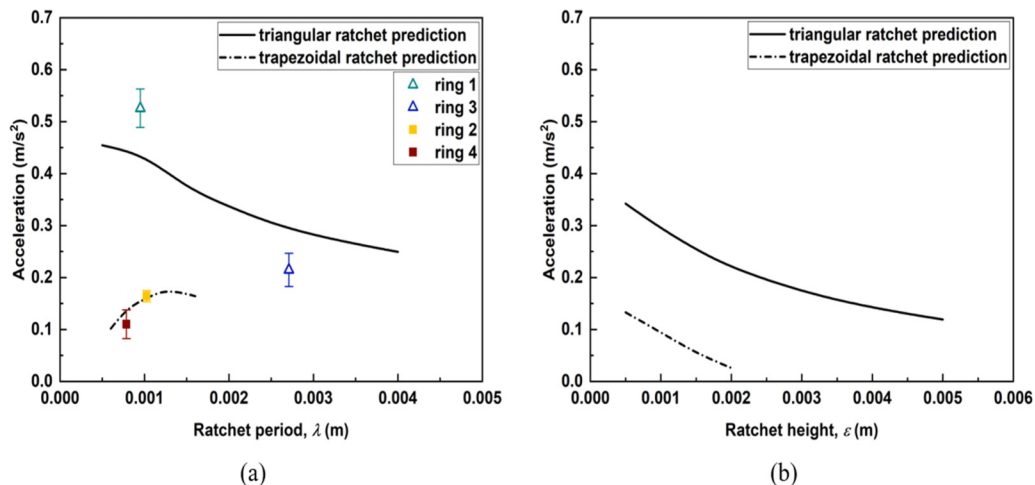


FIG. 5. Effect of ratchet parameters on initial acceleration predicted by the model. (a) Effect of ratchet period, where $\varepsilon = 0.5$ mm. (b) Effect of ratchet height, where $\lambda = 1.5$ mm. The trapezoidal ratchet model was plotted with a flat top ratio of $\lambda_c/\lambda = 0.145$.

their contact area, thus increasing the driving force as well as the surface energy. The surface tension takes a dominant role in maintaining a stable droplet height since the shear force only acts beneath the droplet. For example, for a droplet with $R \sim 3$ mm, the shear force and surface tension are ~ 25 and ~ 354 μN , respectively [2]. Surface tension and gravity are mainly responsible for restoring the “normal” droplet shape [18], especially small droplets that do not have a constant height.

When the ratchets are designed with comparable period and height (such that $\lambda_{e,o} \sim \varepsilon$), the driving force and acceleration will become weaker because the droplet deformation becomes more symmetrical (i.e., where $C_1 \approx 0.5$), which reduces the AC vapor flow distance, and therefore the shear force acting on the droplet is reduced. Additionally, trapezoidal ratchet designs [Fig. 3(c)] will further reduce the effective driving force acting on the whole droplet. This can be seen by comparing Fig. 4(a) (triangular ratchets) with Fig. 4(b) (trapezoidal ratchets). On the flat top of a trapezoidal ratchet, the vapor is assumed to flow “backwards” (against the vapor flow from A to B), since the large space in the ratchet corner allows much lower flow resistance than the “forward” direction (from A to B) [2] (see Fig. S8). As already discussed, small droplets change their trajectory as they accelerate [Fig. S6(a)]. Since ring design 4 transitioned from triangular to trapezoidal ratchets between the inner and outer edges, respectively (Table I), the model predicted a large deviation between acceleration at each edge [Figs. 4(d) and S7]. In addition, the result shows insignificant differences in terms of temperature, as already discussed in the derivation of the model.

For small droplets on ring design 3, a smaller number of ratchets were covered by the droplets because of the larger ratchet period, resulting in the energy loss (friction) to become dominant [19]. This explains the deviation at volumes ≤ 200 μL as observed in Fig. 4(c).

Figure 5(a) plots the acceleration predicted by the model as a function of the ratchet period for triangular-shaped and trapezoidal-shaped ratchets. As clearly shown, for triangular ratchets, a smaller ratchet period improves the driving force and acceleration. The experiment result from two different designs follows the model prediction to a reasonable degree, given that the acceleration measurement on ring design 1 was influenced by the initial elongated droplet shape [see Fig. 3(a)]. For trapezoidal ratchets, the model predicts a much smaller effect of the ratchet period, which still agrees with the experimental observations. Figure 5(b) plots the acceleration predictions as a function of the ratchet height, showing a similar decreasing acceleration for both triangular-shaped and trapezoidal-shaped ratchets when the ratchet period was kept the same. This is likely because as

the ratchet height decreases the gradient of the slope also decreases, which then reduces the driving force.

We found that the terminal velocity of the droplets tended to increase with increasing droplet volume, reaching a plateau of ~ 0.39 m/s. Previous studies found a maximum velocity of ~ 0.35 m/s for a small droplet ($40 \mu\text{L}$), whereas the values decreased to 0.18 – 0.25 m/s when the volume increased to $600 \mu\text{L}$ [21–23]. However, these literature values may not represent the true terminal velocity. According to our experiments, a total travel distance of ~ 242 mm was necessary for a $50\text{-}\mu\text{L}$ droplet to reach its terminal velocity (~ 0.30 m/s), while a displacement of ~ 358 mm was needed for a $385\text{-}\mu\text{L}$ droplet (~ 0.38 m/s). This is much longer than the plates used by Arter *et al.* [22] and Dodd *et al.* [23]. Therefore, one of the advantages of the annular ring design used in this research is droplets over a wider range of volumes are able to be propelled to their terminal velocity, where the effects of the ratchet design parameters [which heavily influence the terminal velocity according to Eq. (16)] can then be elucidated.

In this study we have presented a quantitative way to understand the motion of Leidenfrost droplets on ratcheted surfaces that supersedes the previous scaling analysis, validated by the good agreement between experiment data and the model. Here we have also considered the effect of liquid deformation, derived from a modified vapor flow direction, force balance, and geometry derivation. Our model shows that acceleration is independent of the droplet volume for a broad range of conditions, suggesting that the driving force is exactly scalable with the droplet mass. The ratchet parameters (particularly the height and length) are the key parameters to influence the dynamics. They may also make a difference to the deformation distribution according to our experiment observations. On these compact rings, large slugs are observed to self-propel at terminal velocities as high as 0.39 m/s. The experiments indicate little dependence on the operating temperature, in line with our model's prediction. This model can be used to refine the design of Leidenfrost energy harvesting and fluidic microreactor devices.

ACKNOWLEDGMENTS

G.W. is grateful for the financial support from China Scholarship Council (201704910870) and postgraduate research group in Newcastle University. We also thank the anonymous reviewees, who corrected a couple of faulty analysis in our initial manuscript and helped us rule out more in-depth deformation analysis.

-
- [1] H. Linke, B. J. Alemán, L. D. Melling, M. J. Taormina, M. J. Francis, C. C. Dow-Hygelund, V. Narayanan, R. P. Taylor, and A. Stout, Self-propelled Leidenfrost Droplets, *Phys. Rev. Lett.* **96**, 154502 (2006).
 - [2] G. Lagubeau, M. L. Merrer, C. Clanet, and D. Quéré, Leidenfrost on a ratchet, *Nat. Phys.* **7**, 395 (2011).
 - [3] A. Würger, Leidenfrost Gas Ratchets Driven by Thermal Creep, *Phys. Rev. Lett.* **107**, 164502 (2011).
 - [4] G. Dupeux, M. Le Merrer, G. Lagubeau, C. Clanet, S. Hardt, and D. Quéré, Viscous mechanism for Leidenfrost propulsion on a ratchet, *EPL* **96**, 58001 (2011).
 - [5] G. Wang, J. R. McDonough, V. Zivkovic, T. Long, and S. Wang, From thermal energy to kinetic energy: Droplet motion triggered by the Leidenfrost effect, *Adv. Mater. Interfaces.* **8**, 2001249 (2021).
 - [6] S. Hardt, S. Tiwari, and T. Baier, Thermally driven flows between a Leidenfrost solid and a ratchet surface, *Phys. Rev. E* **87**, 063015 (2013).
 - [7] T. Baier, G. Dupeux, S. Herbert, S. Hardt, and D. Quéré, Propulsion mechanisms for Leidenfrost solids on ratchets, *Phys. Rev. E* **87**, 021001(R) (2013).
 - [8] G. G. Wells, R. Ledesma-Aguilar, G. Mchale, and K. Sefiane, A sublimation heat engine, *Nat. Commun.* **6**, 6390 (2015).
 - [9] P. Agrawal, G. G. Wells, R. Ledesma-Aguilar, G. McHale, A. Buchoux, A. Stokes, and K. Sefiane, Leidenfrost heat engine: Sustained rotation of levitating rotors on turbine-inspired substrates, *Appl. Energy* **240**, 399 (2019).

- [10] See Supplemental Material at <http://link.aps.org/supplemental/10.1103/PhysRevFluids.7.033602> to access movie 1, and for all steps of the model deviation, as well as Fig. S2: model validation using literature data; Fig. S3: how the droplet acceleration was measured; Fig. S4: calibration of droplet volume; Fig. S5: an empirical model of the droplet height; Fig. S7: separate model predictions for ring design 4 based on the droplet's trajectories in Fig. S6; Fig. S8: an assumption of the vapor flow on a trapezoidal ratchet; Fig. S9: droplet terminal velocities.
- [11] Á. G. Marín, D. Arnaldo del Cerro, G. R. B. E. Römer, B. Pathiraj, A. Huis in 't Veld, and D. Lohse, Capillary droplets on Leidenfrost micro-ratchets, *Phys. Fluids* **24**, 122001 (2012).
- [12] T. R. Cousins, R. E. Goldstein, J. W. Jaworski, and A. I. Pesci, A ratchet trap for Leidenfrost drops, *J. Fluid Mech.* **696**, 215 (2012).
- [13] R. B. Bird, W. E. Stewart, and E. N. Lightfoot, *Transport Phenomena* (Wiley, Chichester, New York, 2007).
- [14] C. T. Avedisian and J. Koplik, Leidenfrost boiling of methanol droplets on hot porous/ceramic surfaces, *Int. J. Heat Mass Transfer* **30**, 379 (1987).
- [15] By neglecting the driving force, we have the force balance $F_{i,1}\cos\beta + F_{i,2}\cos\theta \approx m_i g$ in vertical and $F_{i,1}\sin\beta \approx F_{i,2}\sin\theta$ in horizontal, which gives $F_{i,1} \approx (m_i g \sin\theta) / \sin(\theta + \beta)$. The pressure gradient dP/dx acts between points *A* and *C* in Fig. 2. The distance between these points is simply $C_1\lambda/\cos\beta$ by Pythagoras theorem. Therefore, we can approximate the pressure difference as $dP/dx \approx -\Delta P/\Delta x = -F_{i,1}/(A_{i,1}\Delta x)$, as described in Eq. (2).
- [16] We consider the amplitude of the deformed droplet (φ in Fig. 2), where we have $C_1\lambda\tan\beta = C_2\lambda\tan\theta$. Additionally, the proportions of the C_1 and C_2 deformations sum to 1: $C_1 + C_2 = 1$. These relations give $C_1 = \sin\theta\cos\beta / (\sin(\theta + \beta))$ to simplify the result in Eq. (3).
- [17] B. Anne-Laure, C. Clanet, and D. Quéré, Leidenfrost drops, *Phys. Fluids* **15**, 1632 (2003).
- [18] D. Quéré, Leidenfrost dynamics, *Annu. Rev. Fluid Mech.* **45**, 197 (2013).
- [19] G. Dupeux, M. Le Merrer, C. Clanet, and D. Quéré, Trapping Leidenfrost Drops with Crenulations, *Phys. Rev. Lett.* **107**, 114503 (2011).
- [20] C. A. Schneider, W. S. Rasband, and K. W. Eliceiri, NIH Image to ImageJ: 25 years of image analysis, *Nat. Methods* **9**, 671 (2012).
- [21] J. Ok, E. Lopez-Oña, D. Nikitopoulos, H. Wong, and S. Park, Propulsion of droplets on micro- and sub-micron ratchet surfaces in the Leidenfrost temperature regime, *Microfluid. Nanofluid.* **10**, 1045 (2011).
- [22] J. M. Arter, D. J. Cleaver, K. Takashina, and A. T. Rhead, Self-propelling Leidenfrost droplets on a variable topography surface, *Appl. Phys. Lett.* **113**, 243704 (2018).
- [23] L. E. Dodd, P. Agrawal, M. T. Parnell, N. R. Galdi, B. B. Xu, G. G. Wells, S. Stuart-Cole, M. I. Newton, G. McHale, and D. Wood, Low-Friction Self-Centering Droplet Propulsion and Transport Using a Leidenfrost Herringbone-Ratchet Structure, *Phys. Rev. Appl.* **11**, 034063 (2019).